

# Polycrystalline and Single Crystalline NCM Cathode Materials—Quantifying Particle Cracking, Active Surface Area, and Lithium Diffusion

Enrico Trevisanello, Raffael Ruess,\* Gioele Conforto, Felix H. Richter, and Jürgen Janek\*

Representatives of the  $\text{Li}_x\text{Ni}_{1-y-z}\text{Co}_y\text{Mn}_z\text{O}_2$  (NCM) family of cathode active materials (CAMs) with high nickel content are becoming the CAM of choice for high performance lithium-ion batteries. In addition to high specific capacities, these layered oxides offer high specific energy, power, and long cycle life. Recently, the development of single crystalline particles of NCM has enabled even longer lifetimes due to achieving higher Coulomb efficiencies. In this work, the performance of NCM materials with different particle size and morphology is explored in terms of key parameters such as the charge-transfer resistance and the chemical diffusion coefficient of lithium. Cracking of secondary particles leads to liquid electrolyte infiltration in the CAM, lowering the charge-transfer resistance and increasing the apparent diffusion coefficient by more than one order of magnitude. In contrast, these effects are not observed with single-crystalline NCM, which is mostly free of cracks after cycling. Consequently, severe kinetic limitations are observed when cycling large “uncracked” secondary particles at low potential and capacity. These results demonstrate that cracking of polycrystalline particles of NCM is not solely detrimental but helps to achieve high reversible capacities and rate capability. Thus, optimization of CAMs size and morphology is decisive to achieve good rate capability with high-nickel NCMs.

## 1. Introduction

The demand for affordable, high-performance energy storage systems is increasing as electric grids and the automotive industry move toward a sustainable infrastructure.<sup>[1]</sup> Lithium-ion battery technology (LIB) usually is the candidate of choice,

E. Trevisanello, Dr. R. Ruess, G. Conforto, Dr. F. H. Richter, Prof. J. Janek  
Institute of Physical Chemistry  
Justus-Liebig-University Giessen  
Heinrich-Buff-Ring 17, 35392 Giessen, Germany  
E-mail: raffael.ruess@phys.chemie.uni-giessen.de;  
juergen.janek@phys.chemie.uni-giessen.de

E. Trevisanello, Dr. R. Ruess, G. Conforto, Dr. F. H. Richter, Prof. J. Janek  
Center for Materials Research  
Justus-Liebig-University Giessen  
Heinrich-Buff-Ring 16, 35392 Giessen, Germany

 The ORCID identification number(s) for the author(s) of this article can be found under <https://doi.org/10.1002/aenm.202003400>.

© 2021 The Authors. Advanced Energy Materials published by Wiley-VCH GmbH. This is an open access article under the terms of the Creative Commons Attribution-NonCommercial-NoDerivs License, which permits use and distribution in any medium, provided the original work is properly cited, the use is non-commercial and no modifications or adaptations are made.

DOI: 10.1002/aenm.202003400

thanks to its performance specifications, versatility, scalability, and reliability.<sup>[2]</sup> Due to these characteristics, LIBs are now the preferred energy storage device for consumer electronics. Nevertheless, the quest for higher specific energy and power, longer life, and improved safety is far from over.<sup>[3]</sup> The success of the current LIB design encourages continuous evolution of the technology, raising the bar that emerging technologies need to overcome.

In conventional LIBs with intercalation-based cathode active materials (CAMs), the reversible capacity of the cell is limited by the initial concentration of lithium-ions stored in the cathode. Under ideal cycling conditions,  $\text{Li}^+$  ions are shuttled between the CAM and the anode, without any irrecoverable loss. Under practical conditions, side-reactions taking place during normal operation gradually reduce the amount of lithium that can be shuttled between cathode and anode. A natural pathway to improve LIB performance is then to increase the reversible capacity of the cathode active materials.<sup>[4]</sup>

In recent years, lithium cobalt oxide (LCO) as “state-of-the-art” CAM has been increasingly substituted by mixed transition metal oxides, mainly  $\text{Li}_1\text{Ni}_{1-y-z}\text{Co}_y\text{Mn}_z\text{O}_2$  (NCM) and  $\text{Li}_1\text{Ni}_{1-y-z}\text{Co}_y\text{Al}_z\text{O}_2$  (NCA), driven by their lower price and higher specific capacity.<sup>[2,4]</sup> Nickel-rich NCMs and NCAs with low molar concentration of Co, Mn, and Al, i.e., with  $y + z < 0.2$ , and operating at high potentials are now entering the market, with the next targeted material being the unsubstituted  $\text{LiNiO}_2$  (LNO).<sup>[5]</sup> The concepts for mitigation of the fast performance degradation of batteries employing these CAMs are explored in the next section.

Various mechanisms have been proposed to explain the first cycle capacity loss and long-term capacity fading of half-cells containing high nickel NCMs: kinetic limitations at high and low state of charge (SOC),<sup>[6,7]</sup> growth of the cathode electrolyte interphase,<sup>[8]</sup> irreversible transition into electrochemically inactive phases,<sup>[9]</sup> and loss of ionic or electronic contact due to secondary particle cracking.<sup>[9–11]</sup> Until recently, the main strategies employed for mitigating fast capacity fading and extend the lifetime of the cells involved coatings of the secondary particles, doping,<sup>[12,13]</sup> core-shell concepts<sup>[14]</sup> or the use of additives in the formulation of the liquid electrolyte.<sup>[15]</sup> A significant improvement in capacity retention was reported very recently with newly developed “single crystalline (SC)” NCM.<sup>[16–18]</sup> The monolithic microstructure of this new type of CAM, together with

coatings and suitable electrolyte additives, effectively reduced the impact of parasitic processes and secondary particle cracking, significantly increasing the Coulomb efficiency (CE) of full cells.<sup>[16,17]</sup> However, the scarcely reported comparison between the rate capability of polycrystalline (PC) and SC cathodes with similarly sized particles indicates slower kinetics of the single-crystalline materials.<sup>[19]</sup> The relatively slow diffusion of lithium in NCMs hinders relithiation during the discharge process, consequently lowering material utilization and accessible capacity.<sup>[7,20]</sup>

In a previous study, we addressed how liquid infiltration inside the microcracks formed during the first charge leads to a higher apparent lithium diffusion coefficient and shorter pathways for lithium diffusion, consistent with an increase of the electrochemically active surface area and reduction of effective particle size in the cathode materials.<sup>[21]</sup> This was not observed with mechanically rigid solid electrolytes that could not fill the newly created space in the secondary particles. Therefore, crack-free single crystalline CAM is expected to incur similar kinetic limitations even when a liquid electrolyte is employed.

In this work, we explore how the discharge capacity of Ni-rich  $\text{Li}_x\text{Ni}_{0.8}\text{Co}_{0.1}\text{Mn}_{0.1}\text{O}_2$  cathodes is influenced by the microstructure of the CAM and its evolution during cycling. Critical parameters that characterize lithium ion (de)intercalation in the layered oxides are the exchange current density  $i_0$  and the lithium chemical diffusion coefficient  $\bar{D}_{\text{Li}}$ .<sup>[22,23]</sup> These are intrinsic properties of the material and change only as function of the molar fraction of lithium inserted (equivalent to SOC). The experimentally accessible macroscopic quantities linked to these parameters are the charge-transfer resistance  $R_{\text{CT}}$  and the Warburg coefficient  $Z_{\text{W}}$ . These quantities regulate the performance of the cathode in a battery, with low values required for high capacity at high charge/discharge rates. Combining the results from electrochemical and morphological characterization techniques, we provide key insights into the different chemomechanical evolution of single crystalline and polycrystalline CAMs in liquid electrolyte-based LIBs. We then conclude with a brief overview and interpretation of recent literature data in the light of our results, discussing the relationship between shape and size of CAMs and their performance.

## 2. Result and Discussion

### 2.1. Morphological Evolution

A widely reported chemomechanical effect influencing the morphology of high-nickel NCM is the formation of microcracks inside polycrystalline particles upon cycling.<sup>[10,11,24,25]</sup> When more than 75% of lithium is extracted from the material, a step-like decrease of the unit-cell volume leads to the build-up of internal stress in polycrystalline CAMs due to the different orientation of the primary crystallites.<sup>[26,27]</sup> Eventually, the anisotropic contraction initiates the separation of the primary particles and the appearance and growth of microcracks. This was observed in secondary particles as early as during the first charge.<sup>[28]</sup> In contrast, single-crystalline materials seem to not be affected in this way, with CAM particles not showing any major cracks after more than 1000 cycles.<sup>[18]</sup>

In order to confirm that also in “bulk” cathode sheets microcrack formation takes place during the first charge, the morphological features of charged and pristine cathode sheets were compared. Batteries based on both polycrystalline and single-crystalline CAMs were charged to a cutoff potential of 4.2 V and subsequently disassembled. The changes in the morphology of PC and SC cathode active materials before and after this first delithiation can be seen in the cross-sectional focused ion beam combined with scanning electron microscopy (FIB-SEM) images in **Figure 1**. The pristine polycrystalline NCM in **Figure 1a** is dense and does not show any evident gap between the primary crystallites. However, after charging to 3.8 V (**Figure 1b**), fractures start to be visible within the PC particles and upon charging to 4.2 V cracking becomes more severe (**Figure 1c,d**). In contrast, no difference can be seen before and after charge of the single crystal cathode, confirming the mechanical stability of the monolithic particles upon the first delithiation. We note that cracks were also observed for single-crystalline NCM materials when charged to higher potentials.<sup>[29,30]</sup> However, oxygen loss and the resulting damage to the crystal structure can impede lithium diffusion and result in fast

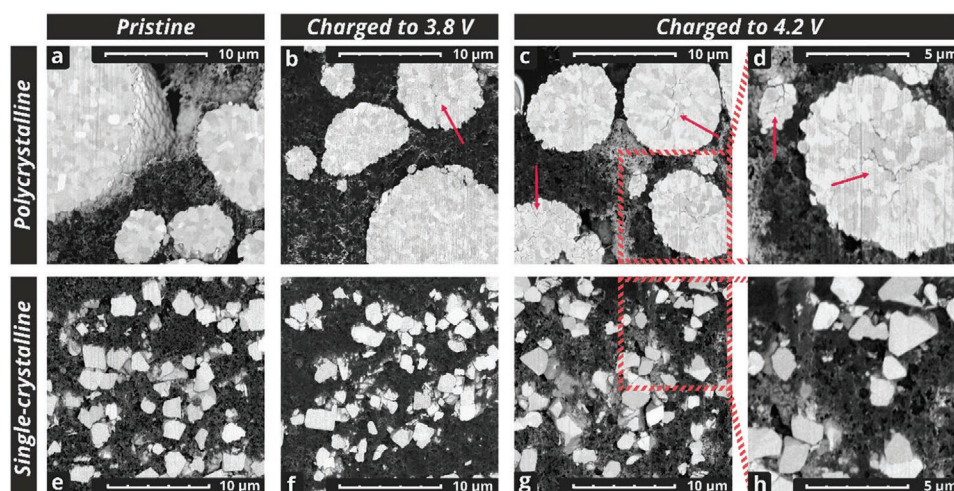


**Figure 1.** a–d) Focused ion beam (FIB) cross-sectional SEM images of cathode sheets in pristine, as-casted conditions (left) and charged to 4.2 V (right) for polycrystalline NCM and e–h) monolithic, single crystalline NCM. The development of gaps, highlighted by red arrows, in the microstructure of the secondary particle is evident in the polycrystalline sample but cannot be observed in the monolithic one.

capacity fading.<sup>[25]</sup> We avoid high potentials in the present study as we focus on CAMs cycled in a practical potential window.

To investigate whether secondary particle cracking causes an increase of the specific surface area, krypton physisorption was used to monitor its evolution in the PC material. The specific surface area of a set of cathodes retrieved from batteries charged to different cutoff potentials was determined with the Brunauer–Emmett–Teller (BET) method (Figure 2a,b). With

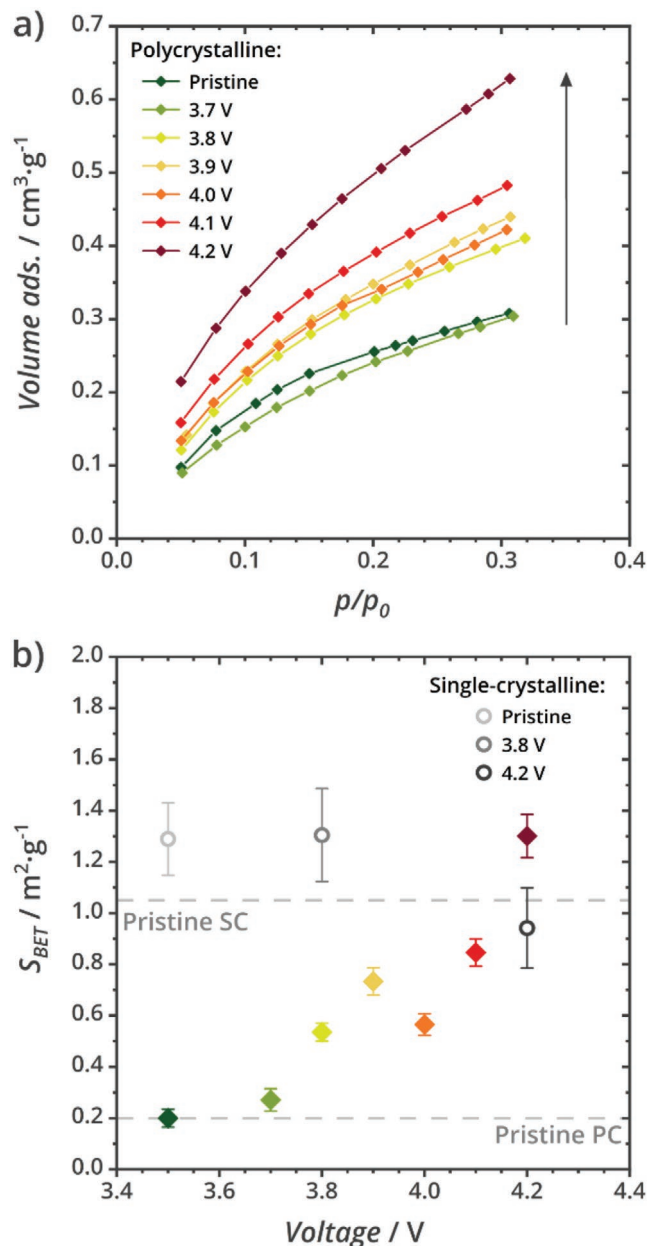


**Figure 2.** a) Krypton physisorption isotherms for a set of PC cathodes recovered from batteries charged to different cutoff potentials and b) BET specific surface areas extracted from these isotherms and the isotherms shown in Figure S1 in the Supporting Information. The gray-shade baselines represent the specific surface area of the pristine NCM single-crystalline (SC) and polycrystalline (PC) powders, used as a reference value to exclude contributions from the binder and conductive carbon. Error bars represent the sample weighing error.

cathodes based on the SC material, no change of adsorbed gas volume and BET area was observed upon charging (Figure S1, Supporting Information, and Figure 2b). On the other hand, the incremental trend of the volume of adsorbed krypton with the SOC of the cathode clearly corresponds to the rise of the calculated BET-area from the initial  $0.2 \text{ m}^2 \text{ g}^{-1}$  of the pristine material to  $\approx 1.4 \text{ m}^2 \text{ g}^{-1}$  for the cathode charged up to 4.2 V versus  $\text{Li}^+/\text{Li}$ . Interestingly, the increase in BET-area already sets off at rather low potentials  $< 3.9 \text{ V}$  versus  $\text{Li}^+/\text{Li}$ , when the internal stress in NCM should be rather low. However, in situ SEM experiments with single-particle electrochemical measurements and acoustic emission measurements confirm significant cracking of high-nickel NCA, NCM, and LNO at relatively low potentials, suggesting that the accumulated internal stress is sufficient to initiate crack formation.<sup>[28,31,32]</sup>

A similar increase of the specific surface area was obtained by Gasteiger et al. by simulating aging effects on polycrystalline NCM with a hydrofluoric acid/electrolyte or water treatment.<sup>[9]</sup> They concluded that electrolyte penetration into these voids, together with  $\text{O}_2$  evolution at high degrees of delithiation, was responsible for the surface degradation of NCM and long-term capacity loss. We hypothesize that not only after multiple cycles but already during the first charge these gaps can be infiltrated by the liquid electrolyte. This would progressively lead to a higher surface area available for the transfer of lithium ions across the liquid electrolyte (LE)|CAM interface. The effect that this phenomenon has on the electrochemical properties of NCM half-cells is investigated in the next section.

## 2.2. Lithium Diffusion Coefficient in NCM

The lithium chemical diffusion coefficient  $\tilde{D}_{\text{Li}}$  is the key parameter that describes the transport of lithium inside the CAM,<sup>[33]</sup> i.e., from the surface to the core of NCM and vice versa. Experimentally, the galvanostatic intermittent titration technique is commonly used for determination of  $\tilde{D}_{\text{Li}}$ , with short polarizations at low specific currents to measure its evolution at smaller intervals of state of charge. This procedure allows the assumption of semi-infinite conditions where  $c_0$ , the initial concentration of lithium in the bulk of the material, is unchanged by the polarization step.<sup>[21,34]</sup> To extract the lithium diffusion coefficient assuming semi-infinite boundary condition, the voltage relaxation measurements were interpreted using the same method as in our previous study.<sup>[21]</sup> Briefly, the open circuit potential  $V_{\text{OC}}$  was assumed to evolve with time according to the following equation

$$V_{\text{OC}}^{s-i}(t) \equiv V_0 - \frac{2}{\sqrt{\pi}} I Z_w \left[ \sqrt{t} - \frac{t}{\sqrt{t}} \right] \quad \text{with} \quad Z_w = \frac{WRT}{z^2 F^2 A c_0 \sqrt{\tilde{D}_{\text{Li}}}} \quad (1)$$

$t_{\text{pol}}$  and  $I$  are the chosen polarization time and current,  $c_0$  is the concentration of lithium before the polarization step, and  $z$ ,  $F$  are the electric charge of the ion and the Faraday constant, respectively. The surface areas  $A$  of both PC and SC pristine materials were determined by BET and assumed constant upon (dis)charging. Thus, the Warburg coefficient  $Z_w$  and the semi-infinite lithium chemical diffusion coefficient  $\tilde{D}_{\text{Li}}^{\text{app}}$  in NCM can be obtained. For a nonstoichiometric

mixed-conducting material such as NCM, the thermodynamic factor is  $W = \frac{\partial \ln(a_{\text{Li}})}{\partial \ln(c_{\text{Li}})}$  and can be calculated from  $V_0$  versus  $c_{\text{Li}}$  data recorded during the experiment, i.e., from the lithium activity as function of the lithium concentration.<sup>[34,35]</sup> This parameter represents the activity change of lithium as a function of the state of charge of the CAM and is therefore morphology independent (Figure S2b, Supporting Information). It has to be noted that this method is only applicable for materials exhibiting a solid solution mechanism for ion (de)intercalation. When this is not the case, the coexistence of two different phases results in a value of  $W$  close to zero, corresponding to the potential “plateau” in the  $V_0$  versus  $c_{\text{Li}}$  data, and thus Equation (1) cannot be used to obtain  $\tilde{D}_{\text{Li}}^{\text{app}}$ . As can be seen in Figure S2b in the Supporting Information, this is not the case for the presently investigated material over a wide range of potentials. High-nickel NCM is typically a single-phase material at different SOC and only in the high potential region two phases might coexist, as highlighted by the rapid drop of  $W$ .<sup>[6,24,33]</sup>

The measured Warburg coefficients normalized to the active mass of CAM on the electrode are shown in Figure 3 for both polycrystalline and single crystalline samples. During the first charge,  $Z_W$  decreases for both NCM materials until  $x$  reaches a value of 0.6, corresponding to a potential of 3.8 V versus  $\text{Li}^+/\text{Li}$ . Subsequently, it continues to decrease in the PC based cathode while it increases in the SC based one. During discharge,  $Z_W$  in the single-crystalline sample strictly follows the trends measured for the first charge. In contrast, the Warburg coefficient of the polycrystalline sample remains low, suggesting that an irreversible change occurred during the first charge. According to Equation (1), lower values of the Warburg coefficient can only be explained by an increased electrochemically active area, as  $W$ ,  $\tilde{D}_i$ , and  $c_0$  depend only on the state of charge. The permanent decrease of the value of  $Z_W$  in the PC cathode, especially at low voltages, suggests that an irreversible morphology change takes place during the first charge in the polycrystalline NCM. In contrast, the single-crystalline NCM shows a fully reversible variation of this coefficient, which suggests that the single-crystalline NCM particles remain intact during cycling.

### 2.2.1. The Chemical Diffusion Coefficient

The extent of this irreversible change in the PC NCM becomes clearer when comparing the evolution of lithium diffusion coefficients of the two CAM morphologies (Figure 4), as calculated with Equation (1). At the beginning of the first charge, both CAMs are characterized by similar  $\tilde{D}_{\text{Li}}^{\text{app}}$  values. Afterward, the increasing concentration of lithium vacancies during delithiation of the CAMs leads to higher diffusion coefficients, in accordance with ab initio calculations and recent NMR results.<sup>[36,37]</sup> Fast migration of lithium ions in layered oxides was shown to be associated with lithium movements through the tetrahedral site, energetically favored over the direct hopping when a pair of lithium vacancies is adjacent to the mobile ion.<sup>[38,39]</sup> In single crystalline NCM  $\tilde{D}_{\text{Li}}^{\text{app}}$  peaks close to a value of  $x \approx 0.5$ , while it continues to increase by more than one order

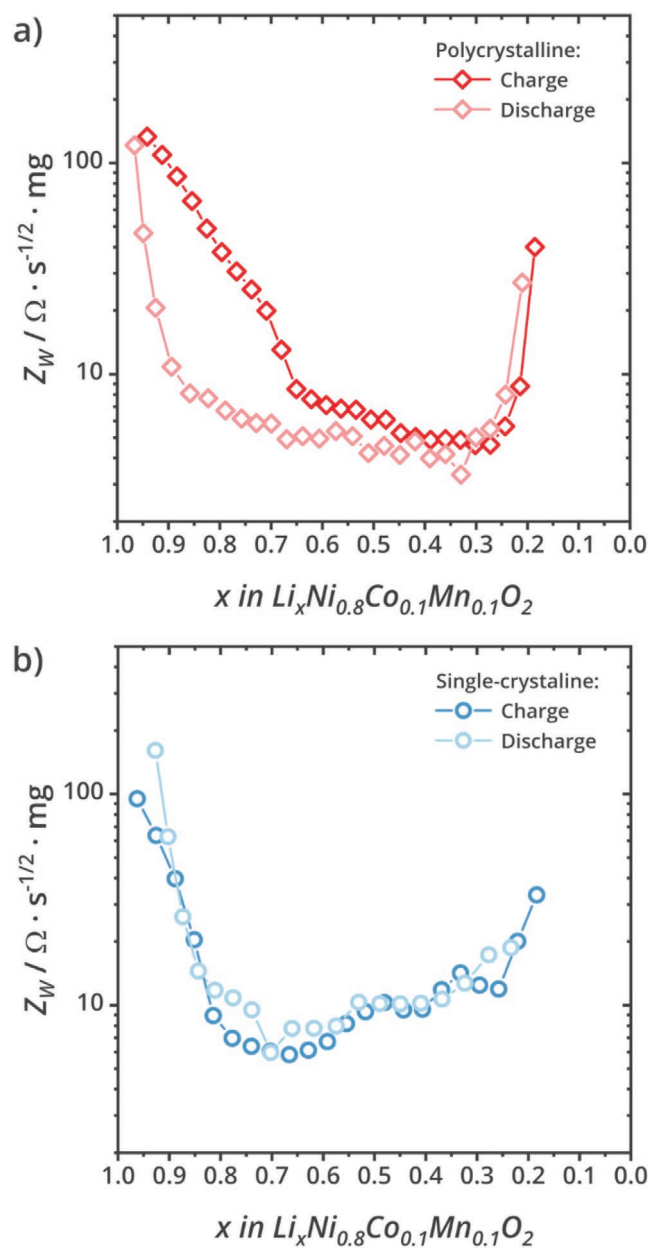


**Figure 3.** Evolution of the Warburg coefficient determined by galvanostatic polarization and relaxation for a) polycrystalline secondary particles of NCM and b) single-crystalline (monolithic) particles of NCM.

of magnitude for polycrystalline NCM when charging to higher potentials. When 70% of the lithium is extracted ( $\approx 4.2$  V vs  $\text{Li}^+/\text{Li}$ ), the diffusion coefficient decreases significantly in both materials, as the transition into the H3 crystal structure narrows the  $\text{Li}^+$  diffusion channels by decreasing the interlayer spacing.<sup>[40]</sup> As previously mentioned, the lower values of  $\tilde{D}_{\text{Li}}^{\text{app}}$  at this potential can be attributed to the coexistence of the H2 and H3 phases and a corresponding value of  $W \rightarrow 0$  (Figure S2b, Supporting Information). In theory, the maximum value for lithium migration via the divacancy mechanism should be obtained when the concentration of vacant and occupied  $\text{Li}^+$  sites is about equal ( $\text{Li}_{0.5} \text{Ni}_{0.8} \text{Co}_{0.1} \text{Mn}_{0.1} \text{O}_2$  at around 3.9 V vs

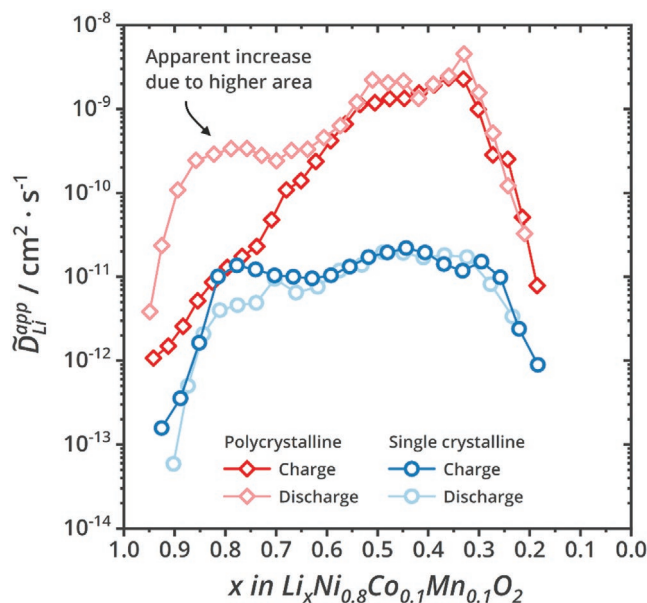


**Figure 4.** Apparent lithium diffusion coefficient  $\tilde{D}_{Li}^{app}$  calculated from the Warburg coefficient during the first charge/discharge cycle for polycrystalline and single crystalline NCM cathodes. As a constant surface area was assumed for both NCM morphologies, this leads to an overestimation of  $\tilde{D}_{Li}$  when cracks in secondary particles are infiltrated by liquid electrolyte, hence the shown diffusion coefficient can be only considered as an apparent value ( $\tilde{D}_{Li}^{app}$ ).

$\text{Li}^+/\text{Li}$ ).<sup>[39]</sup> However, only during discharge both CAM morphologies show the highest  $\tilde{D}_{Li}^{app}$  in the expected region around  $x \approx 0.5$  or 50% of the material utilization.

The discrepancy between the values of  $\tilde{D}_{Li}^{app}$  determined during charge and discharge in PC NCM can be caused by two main factors: a change in the crystal structure (change of  $\tilde{D}_{Li}$  caused by different diffusion dynamics) or an increased surface area (apparent increase of  $\tilde{D}_{Li}^{app}$ ). The two CAM morphologies share the same composition and no two-phase region was observed for NCM811 in this potential window as already discussed above,<sup>[24,37]</sup> therefore their different behavior cannot be caused by a different transport mechanism, i.e., diffusion dynamics, inside the primary particles. Furthermore, very similar  $\tilde{D}_{Li}^{app}$  values for PC and SC were determined at the beginning of the charging process. This confirms that the two morphologies share physicochemical properties, i.e., values of  $W$  and  $\tilde{D}_{Li}$ , suggesting that the structure and composition of both materials is equivalent and that the BET surface area of the pristine powders corresponds to the electrochemically active area in the casted cathode. The only possible explanation for different behavior of the PC NCM is therefore a morphological change happening during the first charge. Thus, we conclude that  $\tilde{D}_{Li}$  obtained in this way for the polycrystalline cathode is an apparent diffusion coefficient,  $\tilde{D}_{Li}^{app}$ , as a constant surface area was used for its calculation. Further, we note that other mechanisms, such as the formation of a cathode–electrolyte interphase or the reconstruction of the surface structure of NCM, are unlikely to cause the high values of  $\tilde{D}_{Li}^{app}$  for PC NCM, as this would rather result in slower kinetics, although improved kinetic parameters are presently observed.

### 2.2.2. Correlation of Surface Area and Apparent Chemical Diffusion Coefficient

According to Equation (1), the sevenfold increase of area  $A$  observed by Kr-physisorption would contribute to a roughly fifty times higher value of  $\tilde{D}_{Li}^{app}$ , given the quadratic relationship between the two parameters. This is in good agreement with the diffusion coefficient presented in Figure 4, with the values during discharge being consistently at least one order of magnitude higher than during the beginning of the first charge. This confirms that the discrepancy between the values of  $\tilde{D}_{Li}^{app}$  obtained during charge/discharge in the PC cells is caused by a morphology-dependent parameter, in this case the change in surface area. Only the infiltration of liquid electrolyte after crack formation can explain the high apparent diffusion coefficient in the PC cathode, with the effect increasing in magnitude at higher state of charge. This interpretation is supported by the increase in specific surface area that already becomes significant at 3.8 V versus  $\text{Li}^+/\text{Li}$  for the PC cathode (Figure 2b), as more primary particles enter in contact with the liquid electrolyte (or Kr during physisorption). Under the assumption that the surface area of PC NCM remains constant at  $1.3 \text{ m}^2 \text{ g}^{-1}$  during discharge (value after completing the first charge, cf. Figure 2b), the surface area of PC NCM during charge can be calculated from the quotient of the respective values of  $Z_w$ , according to Equation (S1) in the Supporting Information. The surface area calculated by this method shows good agreement with the surface area measured by the BET method (Figure S3, Supporting Information). This confirms that the discrepancy between the  $\tilde{D}_{Li}^{app}$  determined for PC and SC CAMs (Figure 4) is a result of the incorrect assumption of a constant surface area for the polycrystalline material.

In the literature,  $\tilde{D}_{Li}$  is mostly measured on polycrystalline samples after several formation cycles.<sup>[41–44]</sup> However, only the surface area of the pristine material is taken into account, leading to underestimation of  $\tilde{D}_{Li}$  due to particle cracking, and reported  $\tilde{D}_{Li}$  values are then often overestimated as a consequence ( $>10^{-10} \text{ cm}^2 \text{ s}^{-1}$ ).<sup>[41–45]</sup> Interestingly, Hong et al. observe a discrepancy between  $\tilde{D}_{Li}$  obtained during charge and discharge, but ascribe it to structural rather than morphological effects.<sup>[45]</sup> However, in this case a similar trend would also be expected for the SC NCM which is clearly not the case (Figure 4). In fact, experiments that were carried out using cathode morphologies that are not significantly affected by cracking, such as  $\text{Li}_x\text{Ni}_{0.8}\text{Co}_{0.2}\text{O}_2$  thin films ( $1 \times 10^{-11} \text{ cm}^2 \text{ s}^{-1}$ ),  $\text{Li}_x\text{Ni}_{0.8}\text{Co}_{0.1}\text{Mn}_{0.1}\text{O}_2$  single crystals ( $7 \times 10^{-11} \text{ cm}^2 \text{ s}^{-1}$ ), or  $\text{Li}_x\text{Ni}_{0.8}\text{Co}_{0.1}\text{Mn}_{0.1}\text{O}_2$  in contact with  $\text{LiPS}_5\text{Cl}$  solid electrolyte ( $6 \times 10^{-12} \text{ cm}^2 \text{ s}^{-1}$ ) determine  $\tilde{D}_{Li}$  to be in the same range as for the present data on SC NCM ( $2 \times 10^{-11} \text{ cm}^2 \text{ s}^{-1}$ ) at comparable degree of lithiation ( $x = 0.4$ ,  $\approx 3.9 \text{ V vs Li}^+/\text{Li}$ ).<sup>[21,46,47]</sup>

### 2.2.3. Processes during First Charge Step

The morphological evolution of PC NCM can be described as the sum of different processes taking place during the first charge. The surface of Ni-rich layered oxides is prone to contamination by lithium and transition metal carbonates, which spontaneously form when the alkaline CAMs are in contact with moisture and  $\text{CO}_2$  in the air.<sup>[48]</sup> Previous reports show how  $\text{Li}_2\text{CO}_3$

decomposition catalyzed by transition metals and electrolyte impurities leads to evolution of gaseous  $\text{CO}_2$  with an onset potential of 3.8 V versus  $\text{Li}^+/\text{Li}$ .<sup>[49–52]</sup> Thus, the interplay between the decomposition of carbonate-based contaminations on the surface and/or grain boundaries at low potentials and the anisotropic expansion at potentials above 4.1 V versus  $\text{Li}^+/\text{Li}$  eventually facilitates the formation gaps and cracks that can be infiltrated by liquid electrolytes. In addition, recent progress in nanoelectrode design shows how ion migration can contribute to the diffusion-controlled mass transport in channels with a dimension comparable to the Debye length.<sup>[53,54]</sup> This could lead to significant transport of  $\text{Li}^+$  in the nano/microchannels filled with liquid electrolyte in the PC cathode, circumventing the slower paths inside the CAM crystals. While further examination is needed to confirm this hypothesis, the combination of surface area measurements and imaging confirms that Ni-rich CAMs show in casted cathode sheets the same cracking during the first delithiation as previously observed in isolated polycrystalline particles.<sup>[55]</sup>

### 2.3. Charge-Transfer Resistance of NCM

An increase in surface area of the polycrystalline CAM should not only lead to lower values of  $Z_W$  but also to an overall reduced charge-transfer resistance between the NCM and the electrolyte. Therefore, to monitor the evolution of the charge-transfer in the cell, potentiostatic electrochemical impedance spectra (EIS) were recorded after each relaxation step (used for the measurement of  $Z_W$ , Figure S4, Supporting Information). The impedance response of the batteries was modeled using the equivalent circuit represented in Figure 5a. At high frequencies, the positive offset of the real part is the “bulk” Ohmic resistance linked to the conductivity of the electrolyte in the separator. The first semi-circle at high to mid frequencies is a superposition of two processes. On the cathode side, it corresponds to the electronic contact between CAM, conductive carbon and aluminum current collector.<sup>[56]</sup> On the anode side, it is linked to the geometrical interface and charge transfer between lithium metal, solid electrolyte interphase (SEI), and electrolyte. These assignments are consistent with previous observations and are confirmed here by measurements with a reference electrode (Figure S5, Supporting Information).<sup>[57,58]</sup> The second contribution was assigned to the charge transfer process between the liquid electrolyte and NCM material,  $R_{CT}^{\text{NCM}}$ . Once lithium has been transferred to (or from) the CAM, it diffuses from (or to) the surface to (or from) the bulk of the material during discharge (or charge, respectively). Hence, a Warburg element is introduced in series. The last element is a capacitor, accounting for the intercalation capacitance of NCM. Its value is proportional to the charge that can be stored in the CAM given the amplitude of the potential excitation applied during the EIS measurement. This was shown to be equivalent to the differential capacity of the material at the chosen potential when EIS is measured to low enough frequencies.<sup>[22]</sup>

#### 2.3.1. Interpretation of EIS Data

An exemplary Nyquist plot of EIS data and the fit obtained with this model is shown in Figure 5b for a half-cell with

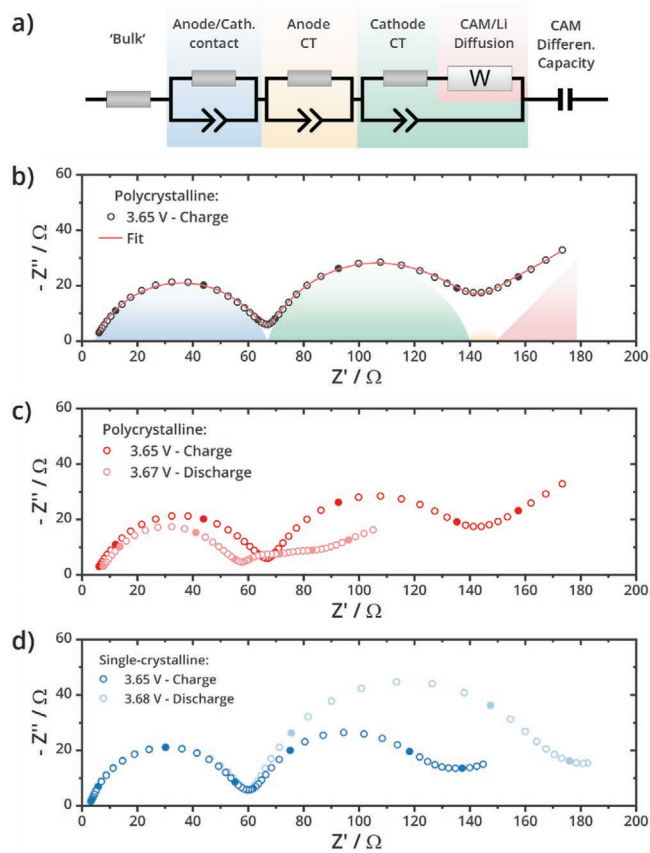


**Figure 5.** a) Equivalent circuit used to describe and fit EIS data of full cells recorded in potentiostatic conditions at a given open circuit voltage (OCV). b) Exemplary Nyquist plot with data and fit according to the previous equivalent circuit. c, d) Nyquist plot of impedance data recorded during the first cycle for polycrystalline and single crystalline cathodes, respectively.

polycrystalline NCM. While this model seems to fit the data well, it cannot reliably separate contributions from the two electrodes. At low frequencies, polarization of the lithium electrode and subsequent Warburg-like diffusion of lithium in the liquid/SEI region is observed. Even though cells employing a reference electrode are better suited to study processes by EIS when other contributions cannot be avoided, it is still possible to use the value of  $Z_W$  obtained from the relaxation as an input parameter ( $W$  in the model in order to fit the impedance response of the full cell, Figure 5a). Other than for the low-frequency diffusion processes, the charge-transfer at the CAM|LE interface can also be reliably obtained from fitting the full cell impedance data as shown in Figure S5 in the Supporting Information.

#### 2.3.2. Correlation of Charge Transfer Resistance and Apparent Diffusion Coefficient

The change in charge-transfer resistance at comparable SOC in the first cycle is shown in Figure 5 for polycrystalline and single-crystalline NCM. At the beginning of the first charge, cells based on the two NCM particle morphologies are characterized by similar impedances, with an almost identical contribution from the NCM-related charge transfer. This confirms

that both cells have well contacted particles and comparable surface areas of cathode material. After charging to 4.2 V,  $R_{CT}^{NCM}$  now appears to be quite different for the two cells when impedance spectra are measured at similar potential during discharge. While the increase in resistance for the cell with single-crystalline NCM can be attributed to surface degradation of NCM at high potential and to electrolyte decomposition, the collapse of the  $R_{CT}^{NCM}$  value observed for the cell with the polycrystalline cathode is caused by the infiltration of liquid electrolyte into the cracks formed during charging. Indeed, the value of the charge transfer resistance decreased from  $\approx 70 \Omega$  before the first charge to a value of  $\approx 15 \Omega$  during discharge, matching well with the increase in surface area determined by BET. This observation is in good agreement with our previous report<sup>[21]</sup> and suggests that cracked NCM particles might have better performance compared to pristine, uncracked ones. This is not only because of the higher surface area but also due to the shorter diffusion length inside the CAM particles. Thus, we stress that the values of  $D_{Li}^{app}$  determined for PC NCM are apparently higher than those of SC NCM due to the unaccounted increase in surface area linked to the change in morphology in the material.

## 2.4. Diffusion Overpotential in NCM

The lithium chemical diffusion coefficient  $\bar{D}_{Li}$  gives direct access to the diffusion overpotential. In the finite diffusion regime (e.g., long polarization times) it can be expressed as

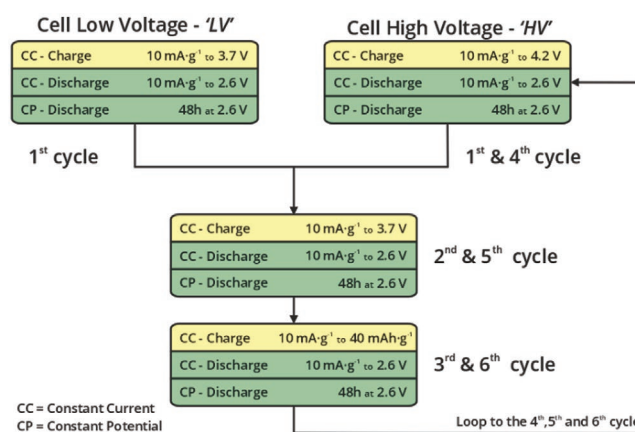
$$\Delta V_{diff}^f(c_{Li}) \cong \frac{1}{3} I Z_w \sqrt{\frac{L^2}{\bar{D}_{Li}}} = \frac{1}{3} I \frac{RT}{F^2} \frac{W}{c_{Li} \bar{D}_{Li} A} \quad (2)$$

where  $L$  and  $A$  are the diffusion layer thickness and the total active area available for charge-transfer in the cathode active material. Two distinct contributions to the magnitude of the diffusion overpotential can be separated with  $c_{Li}$ ,  $W$ , and  $\bar{D}_{Li}$  reflecting the local diffusion mechanism of lithium transport in the CAM and the ratio  $L/A$  ratio accounting for the morphology of the particles. According to Equation (2), the increased contact area after crack formation and infiltration lowers the value of  $L/A$ , as smaller particles with a higher surface area become available in PC cathodes upon charge. In contrast, liquid electrolyte infiltration does not play a role in single crystal NCMs, as they display very limited stress-related change in morphology even after long-term cycling.<sup>[17,18]</sup> Overall, secondary particle cracking leads to lower overpotentials thanks to the decreased values of both  $Z_w$  and charge-transfer resistance. The impact of the cracking of polycrystalline NCM on the cycling performance of full cells will be investigated in the next section.

## 2.5. Kinetic Limitations in NCM During Cycling

### 2.5.1. Limitations in Crack-Free Secondary Particles

The cycling performance of a full battery cell is ultimately limited by the buildup of overpotentials until the cutoff condition



**Scheme 1.** Procedure of the “kinetic test” used to highlight the different performance of polycrystalline cathode active material with and without secondary particle cracking that occurs at high voltage.

is met. As discussed in the previous section, the particle dimension and surface area available for charge transfer directly influence the value of the diffusion overpotential during cycling. For small, uncracked polycrystalline NCM particles (diameter  $< 3 \mu\text{m}$ ), the overpotential would be comparable to similarly sized single-crystals, as the CAMs would have similar surface area and effective particle size. However, in the pristine state the typically large (diameter  $> 5 \mu\text{m}$ ) secondary particles of polycrystalline NCM should exhibit higher overpotentials and worse specific capacities and rate capability compared to cracked NCM, which is characterized by a higher surface area. Therefore, the consequences of secondary particle cracking on the performance of batteries was further investigated in half-cells ( $\approx 1.6 \text{ mAh cm}^{-2}$ , same casted cathode sheet) with different first cycle conditions.

The test procedure is summarized in **Scheme 1**. For polycrystalline NCM, two identical cells were charged at constant current (CC) to cutoff potentials of 3.7 V versus  $\text{Li}^+/\text{Li}$  and 4.2 V versus  $\text{Li}^+/\text{Li}$ , respectively. As a consequence, polycrystalline NCM particles in those cells charged to the higher voltage (HV) were affected by cracks induced by the processes discussed above. In contrast, the CAM in the cells charged to lower voltage (LV) does not experience significant morphological changes like cracking. All cells were discharged with CC and constant potential (CP) steps at 2.6 V to ensure that the maximum amount of lithium could be intercalated, independent of morphology and kinetic limitations. The lower cutoff potential of 2.6 V was chosen to completely fill the Wyckoff position 3a in the structure without overlithiation of the CAM and further transition metal reduction. Overlithiation of the CAM and further transition metal reduction is unlikely at this potential which is further motivated, as also the potential relaxes up to around 2.8 V after the CP step at 2.6 V, which is a typical value of a  $\text{Li}_1\text{Ni}_{0.8}\text{Co}_{0.1}\text{Mn}_{0.1}\text{O}_2$  phase.<sup>[59]</sup>

**Comparison of Low and High Cutoff Potential:** The voltage profiles of the first cycles are shown in **Figure 6a**. The LV battery with a cutoff potential of 3.7 V reaches a charge capacity of  $18 \text{ mAh g}^{-1}$ , but only  $4 \text{ mAh g}^{-1}$  can be discharged in the galvanostatic step. However, the missing  $12 \text{ mAh g}^{-1}$  are recovered during the constant potential step, indicating that the

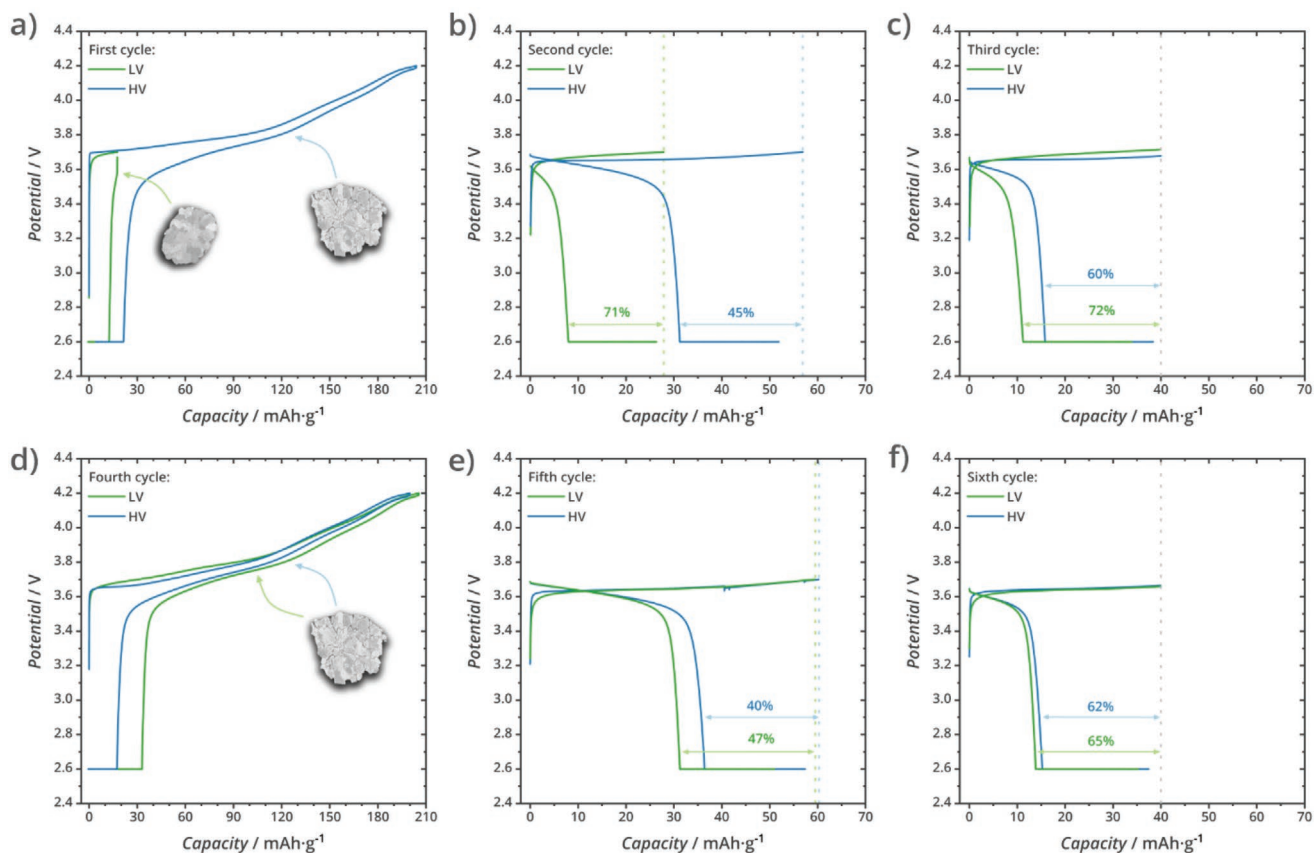


**Figure 6.** Results of the test described in Scheme 1 for cracked (HV cell) and crack-free (LV cell) polycrystalline NCM. Extracts from FIB-SEM images and arrows elucidate the connection between the morphological state of the particles to the voltage/capacity curves. a–f) Voltage profiles as function of the specific capacity recorded for the HV and LV cells in each step of Scheme 1.

initial capacity loss is due mostly to the sluggish lithium diffusion in NCM for this cell. On the other hand, the HV cell charged to 4.3 V reaches a capacity of 204 mAh g<sup>-1</sup> and delivers 183 mAh g<sup>-1</sup> during discharge. After the potentiostatic step, the total discharge capacity for this battery is 200 mAh g<sup>-1</sup>. In the first high voltage cycle, only 4 mAh g<sup>-1</sup> are lost in irreversible side reactions, corresponding to ≈2% of the specific capacity of the cell. Further, this confirms that the total Faraday efficiency during the first cycle is close to 100% showing that non-Faradaic reactions should not have an impact on the determined kinetic parameters. Minor differences in the voltage profiles were recorded at the beginning of each charge, but, after ≈15 mAh g<sup>-1</sup> were transferred, the overpotential was similar for both cells. Measurements employing a reference electrode confirmed that this discrepancy is likely caused by the impedance of the Li|LE interface between lithium metal and liquid electrolyte. As can be seen in Figure S6 in the Supporting Information, the impedance of the Li|LE interface is initially very high, but rapidly decreases after some lithium is plated during the first charge and the final overpotentials associated with this interface can be neglected. Thus, charge and discharge capacities as well as Coulomb efficiencies should not be affected by the initial kinetics at the Li|LE interface.

In the second cycle, both cells are charged to a cutoff voltage of 3.7 V under constant current condition. The corresponding

voltage profiles are shown in Figure 6b. While 57 mAh g<sup>-1</sup> could be transferred from the HV cell, only 27 mAh g<sup>-1</sup> could be transferred from the LV cell due its higher overpotential. Even with the cycling conditions unchanged, the capacity of the LV cell increased compared to its previous cycle. This suggests that even when batteries are charged to low SOC, improvements in the cathode/anode interfaces lead to higher accessible capacities. After the successive discharge step at constant current, with a Coulomb efficiency of 55% the HV cell again outperformed the LV one, with a CE of 29%. The lower value for the LV cell is clearly linked to its higher overpotential. A comparative test was performed with cells based on SC NCM (Figure S7a,b, Supporting Information). Clearly, the different first cycle in SC materials does not play a role in the capacity charged in the second cycle, as the two cells reach the same specific capacity with very similar overpotentials, independent of the history of the cathode material. Upon discharge in the second cycle of cells based on SC NCM, the LV cell outperforms the HV cell, with Coulomb efficiencies of 61% and 52%, respectively. This strongly contrasting behavior between PC NCM and SC NCM again confirms the beneficial effect of cracking on the overall performance of LIBs.

After the constant potential step in Figure 6b, the overall CEs for the LV and HV cell with PC NCM are 95% and 92%, respectively. The trend seen in the first cycle repeats here: stronger

kinetic limitations in the LV cell lower the accessible capacity during galvanostatic cycling, but most of the “lost” capacity is recovered when holding at the cutoff potential at the end of discharge. At the same time, the higher surface area of the cracked NCM leads to overall lower CE after potentiostatic steps due to increased contributions of side reactions. Interestingly, the additional capacity accessed during the subsequent constant voltage step in the second cycle was quite close for the two cells, with 18 mAh g<sup>-1</sup> recovered by the LV and 21 mAh g<sup>-1</sup> recovered by the HV cell. This suggests that a steep increase of the diffusion overpotential at composition Li<sub>0.9</sub>Ni<sub>0.8</sub>Co<sub>0.1</sub>Mn<sub>0.1</sub>O<sub>2</sub> limits the discharge capacity, independent of the history of the cell (i.e., presence of cracks). This possibility can be excluded by charging both batteries to the same state of charge, instead of the same upper cutoff potential. This step was performed in the third cycle by charging both batteries to 40 mAh g<sup>-1</sup> (Figure 6c). Even in this case, the higher overpotential of the LV cell limits the discharge capacity in comparison to the HV one, with CEs after the galvanostatic step of 28% and 40%, respectively. This shows that the build-up of overpotential during discharge happens at different SOC (i.e., degree of Li<sup>+</sup> intercalation) in the two cells, confirming that the morphology of the CAM has a stronger influence than its composition on the galvanostatic cycling performance.

Overall this test shows how the high diffusion overpotential, especially in the LV battery with uncracked PC NCM, limits the cycling performance of NCM under constant current conditions. These results are consistent with our measurements of the low diffusion coefficient below 3.8 V versus Li<sup>+</sup>/Li and results reported by Whittingham et al. on the same cathode material.<sup>[7]</sup> The low Coulomb efficiency of both cells is directly linked to the sluggish transport of lithium ions in the NCM as the number of (di)vacancies decreases while approaching full lithiation. Recently, Chapman et al. proposed that higher charge localization in the transition metal layer may also play an important role in slowing down ionic transport in semiconducting Ni-containing cathodes compared to metallic LCO.<sup>[60]</sup> Indeed, this is not an irreversible capacity loss and a significant portion of it can be recovered by holding the potential at low values after discharge.

### 2.5.2. Limitations in Single Crystals versus Cracked Secondary Particles

Finally, both LV and HV cells with PC NCM were fully cycled up to 4.2 V versus Li<sup>+</sup>/Li (Figure 6d), allowing cracks to form in the CAM of the LV cell as well (for sake of simplicity, we will still refer to it as LV). As the LV cell now undergoes minor irreversible reactions during its first charge to high potentials, a lower overall CE is observed similar to the HV cell, which also showed lower overall CE during its first cycle. We note that irreversible reactions still might have occurred during the cycling of the LV cell in the low potential range further limiting the CE in the 4th cycle. The previous tests were then repeated on the HV and LV cells in the following 5th and 6th cycle, confirming that the irreversible cracking process that takes place at high voltages leads to low overpotentials (Figure 6e,f). The newly cracked CAM in the LV cell performs very closely to HV cell

during the 5th cycle and 6th cycle. While the charge/discharge curves are now very similar, small differences can still be seen at the beginning of each charge. These were again attributed to slightly different history of the cells or differences in Li|LE interfaces of the two batteries.

The lower overpotentials linked to liquid electrolyte infiltration into gaps and cracks of large secondary particles should only be observed on polycrystalline CAMs, as single-crystalline CAMs do not show significant cracking. Therefore, a comparative test was performed with cells based on SC NCM. The results are summarized in Figure S7 in the Supporting Information. Clearly the different first cycle in SC materials does not play a role in the capacity charged in the second cycle, as the two cells reach the same specific capacity with very similar overpotentials, independent of the history of the cathode material. Upon discharge in the second cycle, the LV cell outperforms the HV cell, with Coulomb efficiencies of 61% and 52%, respectively. The difference can be attributed to the increase of the charge-transfer resistance observed in the single-crystalline materials discussed in the previous section. The lower CE of SC NCM in the first cycles at high voltage supports this interpretation, with side reactions taking place mostly during the first charge in this CAM morphology. Such unwanted processes play an important role also in polycrystalline CAMs, but overall the degradation taking place on the surface is shadowed by the positive contribution given by the increase in surface area available for charge transfer.

*Long-Term Influence of Cracking:* Recent studies correlated the loss of capacity in long-term cycling tests on NCM based batteries to cracking of secondary particles.<sup>[10,25]</sup> These can be infiltrated by liquid electrolyte, leading to the formation of inactive phases on the surface of the primary particles<sup>[61]</sup> or loss of electronic contact on the single grains.<sup>[9]</sup> However, even though secondary particle cracking is a major challenge for long-term cycling of many nickel-rich cathode materials,<sup>[9,62]</sup> it initially increases the kinetic performance of large secondary particles. In summary, low overpotentials with ≈10 μm sized polycrystalline NCM particles can be achieved only after cracks are generated by an initial charging process at high potential. Liquid electrolyte penetration into these gaps leads to an increased surface area available for charge transfer, counteracting the intrinsically slow lithium diffusion in NCM materials at low state of charge.

Introducing dopants into the CAM crystal structure might improve the intrinsic parameters controlling its performance, exchange current density and chemical diffusion coefficient of lithium.<sup>[63,64]</sup> Another, more flexible approach to achieve higher specific capacities and fast (dis)charge capabilities is to optimize the morphology of the particles to achieve low charge transfer resistance and low diffusion resistance inside the CAM. This can be done by tuning the morphology of the single-crystals or the primary particles in polycrystalline materials toward smaller aspect ratios  $L/A$  according to Equation (2). In a recent work Kim et al. show comprehensive data where primary particle size, orientation, and doping are optimized to overcome high nickel NCMs diffusion limitations.<sup>[63]</sup> Primary particles with a high aspect-ratio and a size of ≈100 nm achieved high specific capacities (230 mAh g<sup>-1</sup>) and first cycle CE (98%). In good agreement with our results and expectations, the discharge capacity of the materials decreased with increasing grain size due to kinetic limitations at low state of charge.

Understanding the role of cracking on the performance of polycrystalline materials is key to engineer better not only PC CAMs but also single-crystalline (SC CAMs). As we demonstrate, cracked PC NCM effectively behaves like an ensemble of sub-micrometer sized primary particles, with a high surface area exposed to the electrolyte and available for Li<sup>+</sup> (de)intercalation. Our results and literature data suggest that the ideal size of SC materials might depend on the specific application, with small crystals enabling fast charge/discharge rates and bigger, micrometer-sized ones being ideal for long-life lithium-ion batteries.

### 3. Conclusions

In this study, we analyze the chemical diffusion of lithium in high-nickel cathode material NCM-811 with different morphologies. The lithium transport kinetics of NCM secondary particles improves at potentials above 3.8 V versus Li<sup>+</sup>/Li, while monolithic NCM single crystals do not show such an increase. We therefore hypothesize that liquid electrolyte can infiltrate the cracks evolved in the secondary particles already during the first cycle. This results in a significant increase in the electrochemically active LE|CAM contact area, while at the same time shortening the pathways of lithium diffusion in the CAM. With a combination of krypton physisorption measurements and FIB-SEM imaging, we correlate secondary particle cracking with the increase in surface area determined with the BET-method. Second, we investigate how secondary particle cracking influences the kinetically limited performance of half-cells based on layered transition metal oxides. We show that liquid electrolyte infiltration is required to lower the diffusion overpotential at high degree of NCM lithiation and access most of the capacity of such cathodes. Our results suggest that while single-crystalline materials might have the advantage of longer cycling-stability and will help to increase battery lifetime, the intrinsically low lithium chemical diffusion coefficient of Ni-rich cathode materials will prove to be the limiting factor for the rate capability. Therefore, morphology and size optimization of single crystalline CAM will be decisive to achieve fast (dis)charge capabilities often required for adoption in the consumer electronic and electromotive markets.

### 4. Experimental Section

**Materials:** Nickel(II) sulfate hexahydrate (Alfa Aesar, 98%), manganese(II) sulfate monohydrate (Alfa Aesar, 99%), cobalt(II) sulfate heptahydrate (Alfa Aesar, 98%), lithium carbonate (>99%, Sigma-Aldrich), lithium metal (Honjo Lithium), NaOH (99%, Sigma-Aldrich), ammonium hydroxide (25% solution, Sigma-Aldrich), gold-coated tungsten wire (25 μm, Goodfellow, UK), 1 M LiPF<sub>6</sub> in a 1:1 vol% of ethylene carbonate: diethyl carbonate (BASF), 1-methyl-2-pyrrolidinone (NMP) (99.5%, Sigma-Aldrich), polypropylene (PP)-separators (2500, Celgard), glass fiber separators (Albet LabScience GF50), and polycrystalline secondary particles of NCM were provided by Volkswagen AG.

**Synthesis of Single Crystal Li<sub>1</sub>Ni<sub>0.8</sub>Co<sub>0.1</sub>Mn<sub>0.1</sub>O<sub>2</sub>:** In an air-tight round bottom flask, precursor Ni<sub>0.8</sub>Co<sub>0.1</sub>Mn<sub>0.1</sub>(OH)<sub>2</sub> powders were precipitated from a 2 M solution of transition metal sulfates by simultaneous addition of 2 M NaOH (aq) and 1 M NH<sub>4</sub>OH (aq) at 60 °C over the course of 2 h with an approximately stirring speed of 450 rpm. During the coprecipitation the pH was kept between 9.5 and 10.5, a continuous Ar

flux was present to avoid the oxidation of metal ions or the precipitation of carbonates. After precipitation, the powders were filtered, washed with deionized water, and dried at 120 °C in a vacuum oven (BÜCHI). Subsequently, 2 g of Ni<sub>0.8</sub>Co<sub>0.1</sub>Mn<sub>0.1</sub>(OH)<sub>2</sub> and 1.57 g of Li<sub>2</sub>CO<sub>3</sub> (Li/transition metal (TM) ratio of 2.1) were mixed in an agate mortar. The mixture was then calcined in oxygen atmosphere (150 cm<sup>3</sup> min<sup>-1</sup>) by heating it at 100 K h<sup>-1</sup> to 875 °C, with a holding time of 6 h. The product was crushed in mortar and 1 g of powder was ultrasonicated in 20 mL of deionized water to separate the NCM particles and to remove excess Li<sub>2</sub>CO<sub>3</sub>. After centrifugation, the liquid phase was discarded and the recovered NCM crystals were heated in oxygen atmosphere at 600 °C for 3 h. The quality of the CAMs used in this study is confirmed by X-ray powder diffraction (XRPD) and SEM imaging (Figure S8, Table S1, and Figure S9, Supporting Information). The particle size distributions (PSDs) of the CAMs are obtained by analyzing SEM images using the ImageJ software and are reported in Figure S10 in the Supporting Information. The surface areas calculated from the PSDs assuming spherical geometry are 0.17 and 0.84 m<sup>2</sup> g<sup>-1</sup> for PC and SC NCM, respectively.

**Cathode Preparation and Cell Assembly:** Cathodes were slurry casted with a doctor blade on aluminum foil. The slurry composition given as mass ratios were 90:5:5 for NCM, poly(vinylidene fluoride) binder (Solef 5130 polyvinylidene fluoride (PVDF), Solvay), and carbon (Super P, TIMCAL), respectively, in NMP. The slurry was tape casted with a doctor blade (250 μm gap) at a speed of 15 cm min<sup>-1</sup>. The printed electrodes were vacuum dried at 120 °C overnight.

Coin cells (CR2032) were assembled inside an argon-filled glovebox. Starting from the lithium metal anode (thickness 200 μm, diameter 14 mm), electrochemical half-cells were assembled by stacking the separator (diameter 16 mm) and the cathode sheet (≈8 mg<sub>NCM</sub> cm<sup>-2</sup>, diameter 12 mm) on it. Before cathode placement, 50 μL of liquid electrolyte was infiltrated into the separator.

Three-electrode cells were assembled in pouch bags by embedding a gold-plated tungsten wire reference electrode, details of which can be found in refs. [57,58]. Briefly, starting from a cathode square (≈8.8 mm<sup>2</sup>), two glass fiber separators (diameter 14 mm) and lithium metal anode (diameter 12 mm) were stacked and placed between aluminum (cathode) and copper (anode) current collectors. The gold-plated wire was placed between the two separators and each of them was filled with 35 μL of liquid electrolyte during cell stacking. The lithiation process of the reference wire was carried out prior to the polarization-relaxation measurements at 25 °C.

**Electrochemical Characterization:** Galvanostatic polarization and relaxation measurements were carried out to determine the lithium diffusion coefficient in the cathode materials, employing coin cells for all the data reported in the main text. Three-electrode cells were used to confirm the correctness of the models and their data are provided in Figures S1 and S2 in the Supporting Information. Semi-infinite diffusion conditions were employed: A 2 h charging step with a current of 4 mA g<sub>NCM</sub><sup>-1</sup> was followed by a 2 h relaxation step at open circuit voltage. After each relaxation step, EIS were recorded. The polarization, relaxation, EIS sequence was repeated until the battery potential reached 4.3 V during polarization. Afterward, the same procedure was performed with a discharge current of 4 mA g<sub>NCM</sub><sup>-1</sup> until the lower cutoff potential of 2.6 V was reached.

Throughout the study, cells were operated at 25 °C. The polarization/relaxation measurements for the determination of the diffusion coefficient were carried out with Biologic VMP-300 or VMP-3 potentiostats, with the EIS measured in potentiostatic mode by applying a single sinusoidal excitation of amplitude 10 mV superimposed to the open-circuit potential in the range of frequency from 1 MHz to 1 mHz with six points per decade. Galvanostatic charge and discharge and potentiostatic discharge of the cells was carried out on a MACCOR battery cycler. The applied voltage and current are specified where the results are discussed.

**Surface Area Determination—Krypton Physisorption:** Coin cells were charged up to potential values between 3.7 and 4.2 V versus Li<sup>+</sup>/Li before being opened with a crimper apparatus inside a glovebox. The recovered cathodes were washed with 100 μL of ethyl methyl carbonate and

vacuum dried at 120 °C overnight. Samples of NCM powder were directly transferred inside the tube and then vacuum dried at 120 °C overnight before measurement. The cathodes were then weighted using a Mettler Toledo PH204S balance, with a practical precision of ±1 mg. Because of the low surface area, krypton physisorption isotherms were measured on an Autosorb iQ station (Quantachrome), operating at 77.35 K. The Brunauer–Emmett–Teller specific surface area was determined by using 11 data points in the range of relative pressure  $p/p_0$  between 0.1 and 0.3. The contribution to the total specific surface area from PVDF, carbon, and aluminum was subtracted as a constant value of 0.76 m<sup>2</sup> g<sup>-1</sup>, obtained as the difference in area between the casted cathode (0.96 m<sup>2</sup> g<sup>-1</sup>) and pristine polycrystalline NCM (0.2 m<sup>2</sup> g<sup>-1</sup>). For comparison, the surface area of the single crystalline NCM powders was determined to be 1 m<sup>2</sup> g<sup>-1</sup>. The specific surface area values determined by BET for the pristine CAMs are in good agreement with the ones obtained from the PSDs, with a slight underestimation for the SC NCM caused by the assumption of spherical geometry in the latter.

**X-Ray Powder Diffraction:** XRPD of the synthesized single-crystals was collected in Bragg–Brentano geometry using a Panalytical Empyrean diffractometer employing Cu K $\alpha$  radiation. Pulse height distribution levels were set between 45% and 100%, with 50% being the energy of Cu K $\alpha$ , in order to reduce fluorescence detection. Diffractograms were collected in a 2 $\theta$  angular range from 15 ° to 70 °, with a (continuous) step size of 0.026° for a time of 450 s. Rietveld refinement was performed with the Fullprof suite, using the hexagonal  $\alpha$ -NaFeO<sub>2</sub> structure, space group *R-3m*, to describe the phase Li<sub>1</sub>Ni<sub>0.8</sub>Co<sub>0.1</sub>Mn<sub>0.1</sub>O<sub>2</sub>. Thermal factors B for the atoms in the positions 3a (Li), 3b (Ni, Co, Mn), and 6c (O) were fixed to 1.2, 0.4, and 0.62 Å<sup>2</sup>, respectively. The shape of the reflections was parametrized using the Pseudo-Voigt function.

**Scanning Electron Microscopy:** A ZEISS Merlin field-effect scanning electron microscope was used to obtain electron images of the powders in the manuscript. The materials were loaded on an adhesive carbon pad. The acceleration voltage was 10 kV, with 1 nA current. Images were collected with a secondary electron detector. Cross-section images of the pristine cathodes and cathodes charged to a certain potential, which were recovered from the cells as described in the Surface area determination—krypton physisorption section, were taken using a FIB-SEM instrument (Tescan XEIA3). A FIB-crater was milled with a 2  $\mu$ A Xe-beam for 60 min, followed by a 20–60 min polishing step using a less intense ion beam (250  $\mu$ A) that swept the area of interest. The images were taken using an acceleration voltage of 3 kV and an emission current of 250  $\mu$ A. Both secondary electrons and back-scattered electrons were detected.

## Supporting Information

Supporting Information is available from the Wiley Online Library or from the author.

## Acknowledgements

The authors thank Boris Mogwitz for the help with FIB-SEM measurements and Rafael Meusch for the measurement of Kr-physisorption isotherms. R.R. and J.J. thank Volkswagen AG for financial support. E.T. and F.H.R. thank the German Federal Ministry of Education and Research (Bundesministerium für Bildung und Forschung) for funding of the project EvaBatt (03XP0134C) and FLiPS (03XP0261).

Open access funding enabled and organized by Projekt DEAL.

## Conflict of Interest

The authors declare no conflict of interest.

## Data Availability Statement

Research data are not shared.

## Keywords

BET, cracking, lithium-ion batteries, NCM, single-crystals

Received: October 27, 2020

Revised: February 1, 2021

Published online: March 24, 2021

- [1] D. Larcher, J. M. Tarascon, *Nat. Chem.* **2015**, *7*, 19.
- [2] S. T. Myung, F. Maglia, K. J. Park, C. S. Yoon, P. Lamp, S. J. Kim, Y. K. Sun, *ACS Energy Lett.* **2017**, *2*, 196.
- [3] R. Schmich, R. Wagner, G. Höppl, T. Placke, M. Winter, *Nat. Energy* **2018**, *3*, 267.
- [4] J. Kim, H. Lee, H. Cha, M. Yoon, M. Park, J. Cho, *Adv. Energy Mater.* **2018**, *8*, 1702028.
- [5] M. J. Lain, J. Brandon, E. Kendrick, *Batteries* **2019**, *5*, 64.
- [6] S. Schweidler, L. de Biasi, P. Hartmann, T. Brezesinski, J. Janek, *ACS Appl. Energy Mater.* **2020**, *3*, 2821.
- [7] H. Zhou, F. Xin, B. Pei, M. S. Whittingham, *ACS Energy Lett.* **2019**, *4*, 1902.
- [8] S. S. Zhang, K. Xu, T. R. Jow, *Electrochem. Solid-State Lett.* **2002**, *5*, A92.
- [9] F. Friedrich, B. Strehle, A. T. S. Freiberg, K. Kleiner, S. J. Day, C. Erk, M. Piana, H. A. Gasteiger, *J. Electrochem. Soc.* **2019**, *166*, A3760.
- [10] S. Schweidler, L. de Biasi, G. Garcia, A. Mazilkin, P. Hartmann, T. Brezesinski, J. Janek, *ACS Appl. Energy Mater.* **2019**, *2*, 7375.
- [11] S. Ahmed, A. Pokle, S. Schweidler, A. Beyer, M. Bianchini, F. Walther, A. Mazilkin, P. Hartmann, T. Brezesinski, J. Janek, K. Volz, *ACS Nano* **2019**, *13*, 10694.
- [12] T. Weigel, F. Schipper, E. M. Erickson, F. A. Susai, B. Markovsky, D. Aurbach, *ACS Energy Lett.* **2019**, *4*, 508.
- [13] D. Weber, D. Tripković, K. Kretschmer, M. Bianchini, T. Brezesinski, *Eur. J. Inorg. Chem.* **2020**, *3*, 3115.
- [14] P. Hou, H. Zhang, Z. Zi, L. Zhang, X. Xu, *J. Mater. Chem. A* **2017**, *5*, 4254.
- [15] D. S. Hall, R. Gauthier, A. Eldesoky, V. S. Murray, J. R. Dahn, *ACS Appl. Mater. Interfaces* **2019**, *11*, 14095.
- [16] J. Li, A. R. Cameron, H. Li, S. Glazier, D. Xiong, M. Chatzidakis, J. Allen, G. A. Botton, J. R. Dahn, *J. Electrochem. Soc.* **2017**, *164*, A1534.
- [17] J. E. Harlow, X. Ma, J. Li, E. Logan, Y. Liu, N. Zhang, L. Ma, S. L. Glazier, M. M. E. Cormier, M. Genovese, S. Buteau, A. Cameron, J. E. Stark, J. R. Dahn, *J. Electrochem. Soc.* **2019**, *166*, A3031.
- [18] Y. Liu, J. Harlow, J. Dahn, *J. Electrochem. Soc.* **2020**, *167*, 020512.
- [19] H. Li, J. Li, X. Ma, J. R. Dahn, *J. Electrochem. Soc.* **2018**, *165*, A1038.
- [20] J. Kasnatscheew, M. Evertz, B. Streipert, R. Wagner, R. Klöpsch, B. Vortmann, H. Hahn, S. Nowak, M. Amereller, A. C. Gentschew, P. Lamp, M. Winter, *Phys. Chem. Chem. Phys.* **2016**, *18*, 3956.
- [21] R. Ruess, S. Schweidler, H. Hemmelmann, G. Conforto, A. Bielefeld, D. A. Weber, J. Sann, M. T. Elm, J. Janek, *J. Electrochem. Soc.* **2020**, *167*, 100532.
- [22] M. Schönleber, C. Uhlmann, P. Braun, A. Weber, E. Ivers-Tiffée, *Electrochim. Acta* **2017**, *243*, 250.
- [23] R. Weber, A. J. Louli, K. P. Plucknett, J. R. Dahn, *J. Electrochem. Soc.* **2019**, *166*, A1779.
- [24] H. H. Ryu, K. J. Park, C. S. Yoon, Y. K. Sun, *Chem. Mater.* **2018**, *30*, 1155.
- [25] L. de Biasi, B. Schwarz, T. Brezesinski, P. Hartmann, J. Janek, H. Ehrenberg, *Adv. Mater. (Weinheim, Ger.)* **2019**, *31*, 1900985.
- [26] J. M. Lim, T. Hwang, D. Kim, M. S. Park, K. Cho, M. Cho, *Sci. Rep.* **2017**, *7*, 39669.
- [27] A. O. Kondrakov, A. Schmidt, J. Xu, H. Geßwein, R. Mönig, P. Hartmann, H. Sommer, T. Brezesinski, J. Janek, *J. Phys. Chem. C* **2017**, *121*, 3286.

- [28] P. C. Tsai, B. Wen, M. Wolfman, M. J. Choe, M. S. Pan, L. Su, K. Thornton, J. Cabana, Y. M. Chiang, *Energy Environ. Sci.* **2018**, *11*, 860.
- [29] G. Liu, M. Li, N. Wu, L. Cui, X. Huang, X. Liu, Y. Zhao, H. Chen, W. Yuan, Y. Bai, *J. Electrochem. Soc.* **2018**, *165*, A3040.
- [30] Q. Lin, W. Guan, J. Zhou, J. Meng, W. Huang, T. Chen, Q. Gao, X. Wei, Y. Zeng, J. Li, Z. Zhang, *Nano Energy* **2020**, *76*, 105021.
- [31] C. Heubner, U. Langklotz, C. Lämmel, M. Schneider, A. Michaelis, *Electrochim. Acta* **2020**, *330*, 135160.
- [32] S. Schweidler, M. Bianchini, P. Hartmann, T. Brezesinski, J. Janek, *Batteries Supercaps* **2020**, *3*, 961.
- [33] R. E. Usiskin, J. Maier, *Phys. Chem. Chem. Phys.* **2018**, *20*, 16449.
- [34] A. Honders, *Solid State Ionics* **1985**, *15*, 173.
- [35] W. Weppner, *J. Electrochem. Soc.* **1977**, *124*, 1569.
- [36] M. D. Radin, S. Hy, M. Sina, C. Fang, H. Liu, J. Vinckeviciute, M. Zhang, M. S. Whittingham, Y. S. Meng, A. van der Ven, *Adv. Energy Mater.* **2017**, *7*, 1602888.
- [37] K. Märker, P. J. Reeves, C. Xu, K. J. Griffith, C. P. Grey, *Chem. Mater.* **2019**, *31*, 2545.
- [38] A. van der Ven, G. Ceder, *J. Power Sources* **2001**, *97–98*, 529.
- [39] A. van der Ven, J. Bhattacharya, A. A. Belak, *Acc. Chem. Res.* **2013**, *46*, 1216.
- [40] M. Bianchini, M. Roca-Ayats, P. Hartmann, T. Brezesinski, J. Janek, *Angew. Chem., Int. Ed. Engl.* **2019**, *58*, 10434.
- [41] S. Cui, Y. Wei, T. Liu, W. Deng, Z. Hu, Y. Su, H. Li, M. Li, H. Guo, Y. Duan, W. Wang, M. Rao, J. Zheng, X. Wang, F. Pan, *Adv. Energy Mater.* **2016**, *6*, 1501309.
- [42] H. Gao, Q. Wu, Y. Hu, J. P. Zheng, K. Amine, Z. Chen, *J. Phys. Chem. Lett.* **2018**, *9*, 5100.
- [43] Z. Li, C. Ban, N. A. Chernova, Z. Wu, S. Upreti, A. Dillon, M. S. Whittingham, *J. Power Sources* **2014**, *268*, 106.
- [44] H. J. Noh, S. Youn, C. S. Yoon, Y. K. Sun, *J. Power Sources* **2013**, *233*, 121.
- [45] C. Hong, Q. Leng, J. Zhu, S. Zheng, H. He, Y. Li, R. Liu, J. Wan, Y. Yang, *J. Mater. Chem. A* **2020**, *8*, 8540.
- [46] M. D. Levi, D. Aurbach, M. A. Vorotyntsev, *Condens. Matter Phys.* **2002**, *5*, 329.
- [47] F. Wang, M. Ge, S. Wi, X. Liu, J. Bai, S. Ehrlich, D. Lu, W. K. Lee, Z. Chen, *Angew. Chem., Int. Ed.* **2020**.
- [48] J. Sicklinger, M. Metzger, H. Beyer, D. Pritzl, H. A. Gasteiger, *J. Electrochem. Soc.* **2019**, *166*, A2322.
- [49] N. Mahne, S. E. Renfrew, B. D. McCloskey, S. A. Freunberger, *Angew. Chem., Int. Ed. Engl.* **2018**, *57*, 5529.
- [50] S. E. Renfrew, B. D. McCloskey, *J. Am. Chem. Soc.* **2017**, *139*, 17853.
- [51] A. T. Freiberg, J. Sicklinger, S. Solchenbach, H. A. Gasteiger, *Electrochim. Acta* **2020**, *346*, 136271.
- [52] T. Hatsukade, A. Schiele, P. Hartmann, T. Brezesinski, J. Janek, *ACS Appl. Mater. Interfaces* **2018**, *10*, 38892.
- [53] K. Fu, S. R. Kwon, D. Han, P. W. Bohn, *Acc. Chem. Res.* **2020**, *53*, 719.
- [54] J. Xiong, Q. Chen, M. A. Edwards, H. S. White, *ACS Nano* **2015**, *9*, 8520.
- [55] D. J. Miller, C. Proff, J. G. Wen, D. P. Abraham, J. Bareño, *Adv. Energy Mater.* **2013**, *3*, 1098.
- [56] M. Ender, A. Weber, E. Ivers-Tiffée, *Electrochem. Commun.* **2013**, *34*, 130.
- [57] F. J. Simon, L. Blume, M. Hanauer, U. Sauter, J. Janek, *J. Electrochem. Soc.* **2018**, *165*, A1363.
- [58] S. Solchenbach, D. Pritzl, E. J. Y. Kong, J. Landesfeind, H. A. Gasteiger, *J. Electrochem. Soc.* **2016**, *163*, A2265.
- [59] C. Usubelli, M. M. Besli, S. Kuppam, N. Jiang, M. Metzger, A. Dina, J. Christensen, Y. Gorlin, *J. Electrochem. Soc.* **2020**, *167*, 080514.
- [60] A. Grenier, P. J. Reeves, H. Liu, I. D. Seymour, K. Märker, K. M. Wiaderek, P. J. Chupas, C. P. Grey, K. W. Chapman, *J. Am. Chem. Soc.* **2020**, *142*, 7001.
- [61] H. H. Sun, A. Manthiram, *Chem. Mater.* **2017**, *29*, 8486.
- [62] H. Li, A. Liu, N. Zhang, Y. Wang, S. Yin, H. Wu, J. R. Dahn, *Chem. Mater.* **2019**, *31*, 7574.
- [63] U. H. Kim, G. T. Park, B. K. Son, G. W. Nam, J. Liu, L. Y. Kuo, P. Kaghazchi, C. S. Yoon, Y. K. Sun, *Nat. Energy* **2020**, *5*, 860.
- [64] J. O. Binder, S. P. Culver, R. Pinedo, D. A. Weber, M. S. Friedrich, K. I. Gries, K. Volz, W. G. Zeier, J. Janek, *ACS Appl. Mater. Interfaces* **2018**, *10*, 44452.